Chemical Engineering Science 150 (2016) 41–53

Contents lists available at ScienceDirect

Chemical Engineering Science

journal homepage: www.elsevier.com/locate/ces

# Micro-model experiments and pore network simulations of liquid imbibition in porous media

Yu Sun, Abdolreza Kharaghani *, Evangelos Tsotsas

*Thermal Process Engineering, Otto von Guericke University, P.O. 4120, 39106 Magdeburg, Germany*

## HIGHLIGHTS

- Wetting experiments with an etched micro model for mixtures of ethanol and water.
- Imbibition kinetics of water mixtures can be described by the Lucas–Washburn.
- Development of a pore network model for spontaneous capillary imbibition.
- Comparison of optical experimental results with pore network simulations.
- Influence of pore structure on the imbibition dynamics by network simulations.

## ARTICLE INFO

*Article history:*
Received 6 December 2015
Received in revised form
20 April 2016
Accepted 29 April 2016
Available online 30 April 2016

*Keywords:*
Microfluidics
Pore network simulations
Spontaneous imbibition
Pore structure

## ABSTRACT

In this study, spontaneous capillary imbibition into an air-filled transparent etched silicon-glass micro-model is investigated by optical imaging under ambient conditions for mixtures of ethanol and water. Images of the micro-model are acquired by a high-speed CCD camera. The binarized images allow us to obtain the overall imbibition kinetics and the time evolution of the phase distribution. A pore network with the structure parameters of the physical micro-model is generated, and a wetting algorithm that combines several pore-level liquid transport rules is developed to simulate the spontaneous imbibition of the liquid mixture into the network. The pore network simulations are able to reproduce the effects observed in the micro-model experiments. The influence of spatially correlated structural features on the imbibition dynamics is studied by further pore network simulations, and pore structures that cause weak or strong capillary imbibition are identified. The results of wetting simulations are shown for situations which cannot be treated by the Lucas–Washburn equation.



## 1. Introduction

The capillary imbibition of water and other liquids into gas-filled porous media occurs in various fields of research, such as soil science (Blunt et al., 2002), oil recovery (Piri and Blunt, 2004; Yadali Jamaloei and Kharrat, 2010), food industry (Saguy et al., 2005), construction (Leventis et al., 2000), and paper coating (Ghassemzadeh et al., 2001; Ghassemzadeh and Sahimi, 2004), to name only a few. The ongoing issue in the study of capillary flow in porous media is to identify how both the physical properties of the penetrating fluid and the structural characteristics of the porous media affect the imbibition kinetics and the properties of the advancing liquid-gas interface. The detailed description of capillary imbibition is usually complicated due to the intricate pore structure of hosting media and the local interaction of interfaces. The quasi-steady state capillary flow in a porous medium made of cylindrical tubes with constant cross-section was quantitatively described more than a century ago (Bell and Cameron, 1906; Lucas, 1918; Washburn, 1921): in a capillary tube, the distance which the liquid has traveled in time $t$ is proportional to the square root of time ($t^{1/2}$) – this relationship is known as the Lucas–Washburn equation. It is derived by combining the Hagen–Poiseuille equation for the viscous flow of a fluid with the Young–Laplace equation for the capillary pressure across the interface between two static fluids. The validity of Lucas–Washburn scaling law has been assessed for capillary imbibition of liquid water into porous media with pore sizes ranging from nanometers (Gruener and Huber, 2009, 2011; Gruener et al., 2012) up to centimeters (Dullien, 1979; Sahimi, 1993, 2011). The same power law has also been observed during the imbibition of water/ethanol droplet mixtures in packed beds of glass beads (Yang et al., 1988; Jazia

* Corresponding author.
*E-mail address:* abdolreza.kharaghani@ovgu.de (A. Kharaghani).

http://dx.doi.org/10.1016/j.ces.2016.04.055
0009-2509/

et al., 2013). Note that the credibility of this scaling law depends on the viscosity of fluids involved during the imbibition process. It is valid for co-current imbibition when the displaced fluid has low viscosity (i.e. the so-called Washburn situation). It is also valid for counter-current imbibition for two viscous fluids since the imbibition proceeds by a self-similar front which is formed with the resistance behind the front being proportional to the distance the front has propagated into the medium. However, it fails for co-current imbibition with two viscous fluids. It also fails for spherical and radial co- and counter-current imbibition, particularly when the front advances outwards (Mason and Morrow, 2013).

Much research work has been done in the development of mathematical models for capillary-driven imbibition (spontaneous imbibition) that take into account the geometrical complexity of pore structures, i.e., pores with noncircular cross-section (Van der Marck et al., 1997; Polzin and Choueiri, 2003; Cai et al., 2014), capillaries with a monotonically varying radius (Young, 2004; Reyssat et al., 2008), and tortuous capillaries with various aperture shapes (Cai et al., 2014), for example. The research publications cited up to here deal with the modeling of imbibition in capillary tubes or in porous structures which are homogeneous at the macroscopic scale. In such porous media, the wetting front propagates uniformly; hence, the problem can be reduced to one space dimension (Kang et al., 2013).

Reyssat et al. (2009) developed a continuum model based on Darcy's law to interpret experimental results of spontaneous liquid imbibition in composite structures made of both fine and coarse porous regions. These regions are arranged side-by-side – either with a positive or a negative porosity gradient in the flow direction – which gives rise to a heterogeneous pore structure at the macroscopic scale. Following previous work, Shou et al. (2014) developed a physics-based analytical model to study the macroscopic behavior of liquid imbibition into a porous structure made of two layers with distinct heights and porosities. Cheng et al. (2015) developed a one-dimensional continuum model to study the spontaneous imbibition of water into air-filled fractured porous rocks. A rock sample with a fracture represents a heterogeneous medium, where the fracture can be considered as a long macro channel inside the porous matrix. Although the analytical results of Cheng et al. reflect fairly accurately the imbibition kinetics in these composite structures, a more detailed model is indispensable to explain the pore-level imbibition dynamics in a physically and numerically sound way. Also note that this continuum-scale approach assumes that both pore structure and liquid distribution can be homogenized for a description with constant or smoothly varying parameters and variables. Therefore, these models are neither suited for percolation phenomena with fractal and discontinuous liquid clusters, nor can porous media be properly described whose sample size is not much larger than pore size (as for thin porous layers), because in both cases the two scales cannot be separated.

In order to account for the structural details of porous media and for the pore-level physics of transport phenomena therein, 2D and 3D pore network models (PNMs) have advanced considerably since the pioneering work of Fatt (1956). A 2D pore network consists of horizontal and vertical throats with statistically distributed cross-sectional areas; the nodes between the throats act as a spatial grid for the computation of fluid pressure fields. With this simple pore structure, the transport dynamics are determined on the pore level. The flow in each throat is of Poiseuille type, and the advancement of the overall imbibition front is driven by the global pressure difference as well as by local fluid mass conservation at each node of the network. The results of PN simulations are reliable only if the real pore space morphology is represented accurately by the pore network. Established 2D and 3D image acquisition and reconstruction techniques are often used to characterize the pore space topology and geometry of real porous media samples, such as serial sectioning imaging (Vogel, 1997), laser confocal microscopy (Montoto et al., 1995), and synchrotron X-ray tomography or micro-tomography (Al-Raoush and Willson, 2005; Wildenschild and Sheppard, 2012; Wang et al., 2012; Beckingham et al., 2013). The structural information obtained from these imaging techniques can be used to generate a pore network model. Recent improvements in the fabrication of transparent micro-models and in high-speed imaging provide a spatial and temporal resolution high enough to track the imbibition process at the pore scale and to obtain quantitative information on the time evolution of the interface. Micro-models are artificial porous media consisting of a microfluidic pore network with prescribed geometry. They have contributed significantly to identifying the fluid flow mechanisms (Lenormand et al., 1983; Yadali Jamaloei and Kharrat, 2010) as well as the transport properties at the pore level (Cheng et al., 2004; Perrin et al., 2006; Karadimitriou and Hassanizadeh, 2012). These mechanisms and properties were subsequently incorporated into pore network models resulting in a more accurate representation of the pore-scale physics (Blunt, 2001; Mahmud and Nguyen, 2006; Joekar-Niasar et al., 2009; Joekar-Niasar and Hassanizadeh, 2012a, 2012b; Lux and Anguy, 2012).

Thompson (Thompson, 2002) demonstrated the great potential of pore network modeling for solving capillary flow problems in disordered fibrous materials. Various prototype fiber networks with, e.g., different network structure, pore spatial correlation, or solid volume fraction, were constructed based on Voronoi diagrams (Voronoi, 1908). Water invasion simulations with a spatially heterogeneous structure were performed under both spontaneous, due solely to capillary forces, and forced at some volume rate of flow conditions. Bazylak et al. (2008) studied numerically and experimentally liquid invasion into heterogeneous pore networks with radial or diagonal pore size gradient. Although similar flow patterns are obtained from simulations and experiments, the numerical model employed ignores the dynamic effects of the water transport. Hence, the structural effects on the imbibition rate cannot be explained by their models. For a comprehensive review on recent developments in spontaneous imbibition refer to (Alava et al., 2004; Mason and Morrow, 2013).

Note that the exact position and shape of the fluid-fluid interface in the pores is often ignored by PNMs, yet it is known to strongly influence the fluid cluster properties during capillary force driven fluid displacement. Direct numerical simulations using level set (Prodanović and Bryant, 2009), lattice-Boltzmann (Porter et al., 2009), and volume-of-fluid (Ferrari and Lunati, 2013; Kharaghani et al., 2013) methods have been able to resolve the sub-pore scale physics and can serve as benchmarks to validate both microscopic pore network and macroscopic continuum models.

In this paper, optical measurements of the spontaneous imbibition of different liquid mixtures of ethanol and water into an etched glass micro-model are presented. The time evolutions of the imbibed liquid volume and of the liquid distribution are determined from two-dimensional images acquired by a high speed CCD camera. A pore network wetting model is briefly recalled (Sun, 2014). The experimental findings are compared to the pore network simulation results. The influence of structural features on the liquid imbibition dynamics is explored by pore network simulations. Finally, prospects for further work, both theoretical and experimental, are discussed.

## 2. Experimental setup and procedure

The experimental setup consists of a microfabricated silicon network, a synchronized data acquisition system, and an imaging

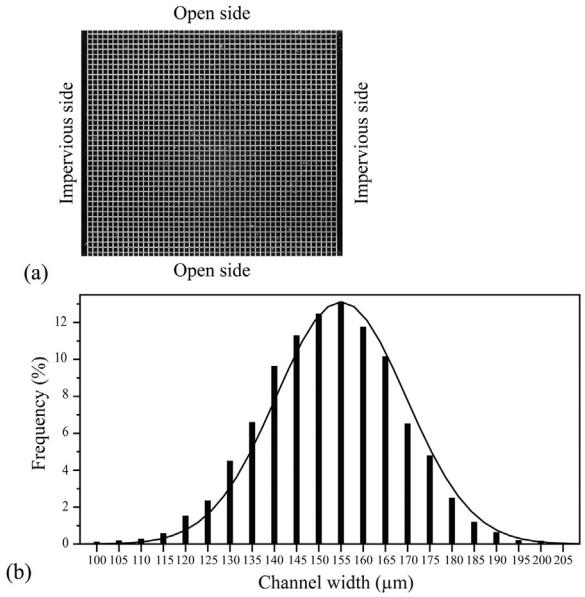


**Fig. 1.** (a) Micro-model, and (b) statistical distribution of designed values of channel widths.

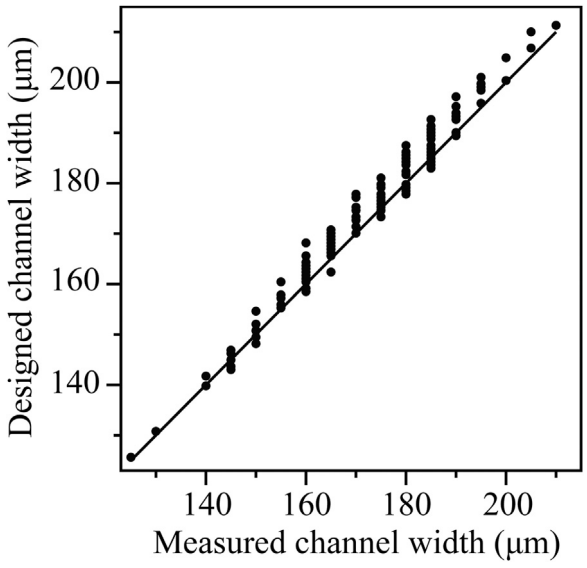


**Fig. 2.** Designed channel widths versus measured channel widths.

processing algorithm. The micro-model for this experiment is chosen primarily because of its transparency, which allows for a relatively straightforward visualization of liquid displacements. The data acquisition system provides sequential images of the microfluidic network as the liquid-gas interface advances. The acquired images are analyzed by an image-processing algorithm to investigate the capillary imbibition kinetics (i.e. the dependence of total saturation on time) inside the micro-model.

### 2.1. Etched silicon micro-model

A quasi-two-dimensional physical micro-model of size $50 \times 46$ flow channels (approximately 49 mm $\times$ 45 mm) is utilized to visually observe the real-time fluid distributions within the channels during the liquid imbibition into the network (Fig. 1a). The micro-model network was manufactured in a clean room by a photolithographic process followed by isotropic wet etching of silicon dioxide ($SiO_2$). Then, the glass structure was sealed by chemical bonding to a silicon (Si) wafer. A key advantage of using silicon in the fabrication of the etched network instead of resin or glass is that it significantly improves the accuracy and roughness of the etched pattern. The micro-model used in this study was produced in collaboration with the institute of Micro and Sensor Systems, Otto von Guericke University, Magdeburg, Germany. Details of the manufacturing process can be found elsewhere (Giordane and Cheng, 2001; Tsakiroglou and Avraam, 2002; Iliescu et al., 2012; Sun, 2014). As indicated in Fig. 1a, the lateral faces of the micro-model are impervious to any fluid, whereas the top and bottom faces are open to ambient air. All flow channels have a length of 1 mm. The widths of flow channels are sampled from a Gaussian distribution with a mean value of 155 μm and a standard deviation of $\pm$ 15 μm (Fig. 1b). The channels lie on a Cartesian lattice and all inner channels have coordination number 4.

Note that the etching technique used for the micro-model fabrication results in an accurate channel length. However, both the channel width and depth depend on the reaction time of the acid solution, which is used to etch the channels into the silicon dioxide. This production step is more difficult to control, and sensitive to the purity and homogeneity of the materials, as well as to environmental conditions. To assess possible manufacturing inaccuracies, the widths of several randomly selected channels were measured from digital microscope images. Fig. 2 shows the widths of selected channels measured from the microscope images and those used in the network design. The comparison shows that the measured channel widths match the designed values well. The deviation of the measured widths from the target values is random, and no apparent spatial correlations are detected; most measured values are below the design values, though. Similarly, the depths of all etched channels were scanned by a non-contact surface profilometer. Out of 4406 channels in total, approximately 99.8% have a depth in the range between 48–53 microns, which indicates a relatively constant channel depth across the entire network. It has been pointed out that the widths and depths of the channels may be inherently correlated due to an isotropic erosion process (Perrin et al., 2006). The depth and width of few channels are measured. It was found that the channel widths and depths are only weakly correlated or nearly independent in this micro-model.

In order to describe the micro-model as a pore network, the void space is divided into pores and throats. A pore is the junction of channels, and a throat is the part of a channel that connects two neighboring pores. Fig. 3a shows a sketch of a part of the micro-model, in which the pores are demarcated by dashed lines. The pores are assumed to be cubic with depth $d$. The pore volume $V_i$ is determined by

$$V_i = d \times \left( w_{im} \times w_{hi} - \frac{w_{hi} - w_{ij}}{2} \times \frac{w_{im} - w_{ni}}{2} \right), \quad (1)$$

where $w_{im}$, $w_{hi}$, $w_{ij}$, $w_{ni}$ denote the widths of the throats *im*, *hi*, *ij*, and *ni*, respectively. The throat length $L_{ij}$ is calculated from the known distance $L$ between the pore centers and from the widths of its perpendicular neighbor throats

$$L_{ij} = L - \frac{w_{im} + w_{qj}}{2}, \quad (2)$$

where $w_{im}$ and $w_{qj}$ denote the widths of the throats *im* and *qj*, respectively. Hence, the throat volume is given by $V_{ij} = L_{ij} \times A_{ij}$, where $A_{ij} = d_{ij} \times (w_{ij} - d_{ij})$ is the throat cross-section area as shown in Fig. 3b. The total void volume of the micro-model obtained in this way is 18.24 $mm^3$.

### 2.2. Imaging system used for the imbibition experiment

A high-speed imaging system (LaVision GmbH) with a 14 bit

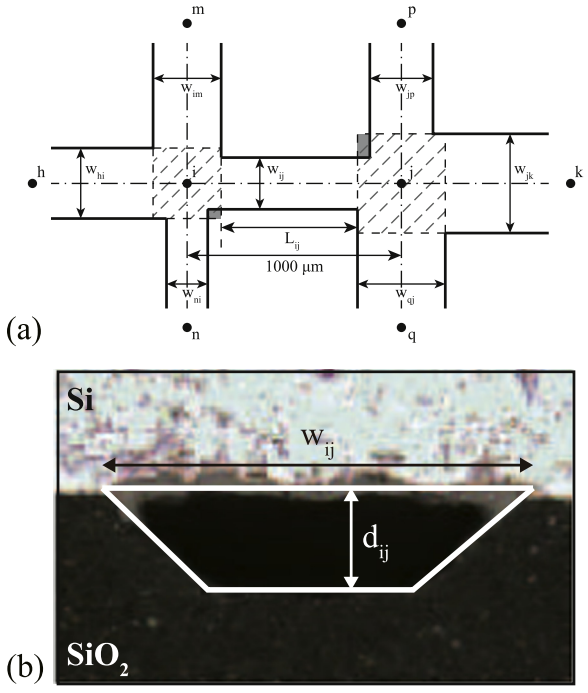


**Fig. 3.** (a) Sketch of a part of the micro-model with geometrical details. Shaded regions show the pores *i* and *j*, and (b) a microscopic image of a flow channel (top view). The white solid lines show the cross section of the channel.

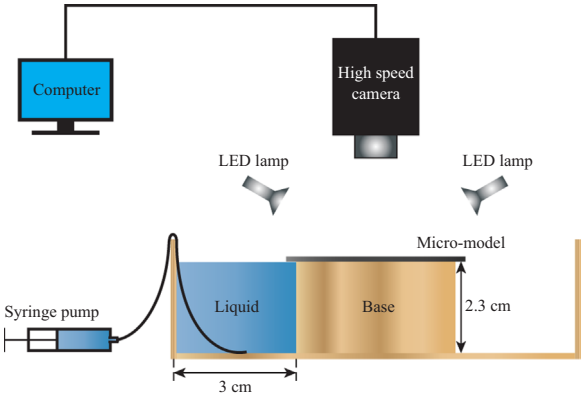


**Fig. 4.** Illustration of the experimental setup designed to visualize the liquid imbibition into an etched glass micro-model.

CCD camera capable of capturing 360 frames per second was employed to acquire two-dimensional images from the top cover of the micro-model (transparent $SiO_2$) during the entire liquid imbibition process; the imaging system is linked to a personal computer as shown in Fig. 4. Due to the limited storage capacity of the camera, a maximum of 9600 images can be continuously recorded for one imbibition measurement. Fig. 4 illustrates the experimental setup. In all measurements, the micro-model was placed horizontally on a ceramic base to prevent effects due to gravitational forces. A liquid reservoir is installed next to the base and filled with a liquid mixture such that its level remains below the micro-model entrance. To initiate liquid imbibition into the micro-model, an additional amount of liquid is carefully injected by a syringe pump into the liquid reservoir until it just touches the micro-model entrance. Then the injection rate is small enough, such that no apparent liquid flow occurs in the reservoir, and the liquid surface remains flat. A lighting system consisting of eight LED lamps in various angles illuminates the micro-model uniformly with relatively constant lighting conditions over time. All components are placed in a darkroom at ambient conditions to exclude external light. This imaging setup provides a good contrast between the dry and wet zones in the micro-model (Fig. 5).

### 2.3. Image processing and analysis

Approximately 6000–7000 images are acquired at a rate of 360 frames per second in each measurement until the micro-model is completely saturated with liquid. The spatial and temporal resolution of these optical images allow for quantitative measurements in systems such as the micro-model described in the previous section. A code was written in Matlab (MATLAB, 2013) to process the raw images. This algorithm is based on four image-processing steps, which are consecutively operated on each image: cropping, binarization, closing, and opening (Serra, 1982). Fig. 5 shows an original grey-scale image and the processed images after each step: first, the raw image is tailored to solely contain the micro-model (cropping, Fig. 5a). A binarization is then performed on the image using a threshold value. Fig. 5b shows the resulting binary image, in which the bright foreground phase indicates empty channels, and the dark background phase indicates wet channels or the solid space between channels. However, a few background pixels are present in the middle of empty channels, due to less reflection and refraction of light from the bottom of channels. In order to eliminate these background pixels, the morphological closing operation is applied to the binary images as seen in Fig. 5c. Furthermore unwanted image elements are caused by air blobs, which may form in channels and which may be trapped there when the liquid enters from both ends of the channel. Our measurements indicate that trapped air bubbles may be stagnant but also advected by the liquid flow. The stagnant air bubbles may act as barriers for the liquid flow, increasing viscous resistance. A possible reason for the air trapping could be attributed to the local topological features of the micro channels. In the binary images, the air bubbles appear as isolated white patches in the (black) liquid saturated zone, and they are removed by the morphological opening operation as shown in Fig. 5d. The influence of the air bubbles present in the micro-model on the capillary imbibition kinetics is beyond the scope of the present publication, but it will be subject to further study.

In order to determine the spatial and temporal evolution of the liquid distribution inside the micro-model during imbibition, the fraction of foreground (white) pixels $\phi$ in $[0,\phi_0]$ in each processed image is calculated. It quantifies the area fraction of empty channels in an image. The fraction $\phi_0$ in the first image is considered as the void fraction of the completely dry micro-model. The liquid saturation $S$ in each image is approximated by $S = 1 - \frac{\phi}{\phi_0}$ and the liquid volume inside the micro-model calculated by $V_L = S \cdot V_T$, where $V_T = 18.24\ \mathrm{mm}^3$ denotes the total void volume of the micro-model.

## 3. Direct observation of spontaneous liquid imbibition

A series of filling kinetics experiments were carried out for three different liquid mixtures of distilled water and ethanol using the experimental procedure described in the previous section. The physical properties of these liquids are shown in Table 1. Here, the values of the equilibrium contact angle are averaged over fifteen measurements by a contact angle goniometer (OCA, DataPhysics Instruments GmbH), which has a resolution of less than 2°. Using this device, the profile of a sessile droplet on a flat glass substrate (the material used for making the micro-model) is measured and thus the contact angle between the liquid-solid interface and the liquid-air interface is determined. The other relevant physical

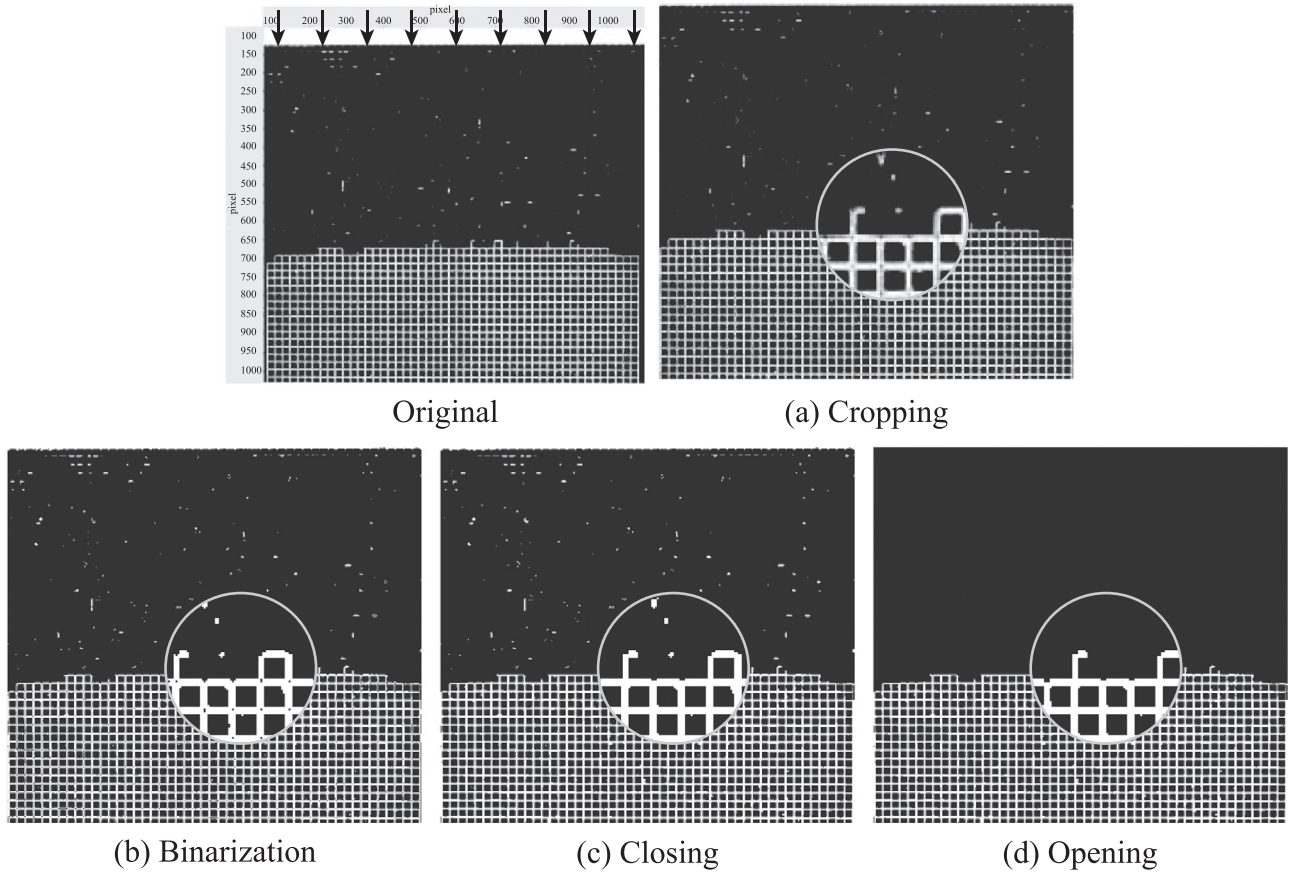


**Fig. 5.** A sequence of image processing steps. Dry and wet regions are shown in white and black, respectively. Arrows indicate the liquid flow from the liquid reservoir into the micro-model.

**Table 1**
Relevant physical properties of ethanol-water mixtures at 20 °C.

| Ethanol [wt%] | Density [kg/m$^3$] | Viscosity [mPa s] | Surface tension [mN/m] | Contact angle [°] |
|---|---|---|---|---|
| 40 | 935.2 | 2.846 | 30.69 | $25.3 \pm 2.4$ |
| 60 | 891.1 | 2.547 | 26.72 | $24.3 \pm 1.7$ |
| 80 | 843.6 | 1.881 | 24.32 | $21.4 \pm 1.2$ |

properties of the ethanol-water mixtures are adopted from the literature (Vázquez et al., 1995; Lide, 2010). An increase in the ethanol concentration results in a larger wetting coefficient (i.e. cosine of contact angle), whereas the surface tension of the mixture decreases.

The sequential images of liquid distributions at different liquid volumes for the mixture of 40% ethanol mass fraction are shown in Fig. 6. Right upon contact of the open facet of the micro model with the surface of the liquid reservoir, the liquid mixture is forced into the micro channels near the cross-sectional area of the micro-model by capillary action. The imbibition process continues while the interface between wet and dry regions slows down until the micro-model is almost fully saturated with the liquid. The liquid penetration in the micro-model appears to occur in a quasi-steady manner with a fairly sharp advancing liquid front. This phenomenon demonstrates that pore-throat sizes only locally influence the imbibition interface morphology. A similar liquid distribution was obtained from the experiments with the same micro-model but different concentrations of ethanol (not shown here).

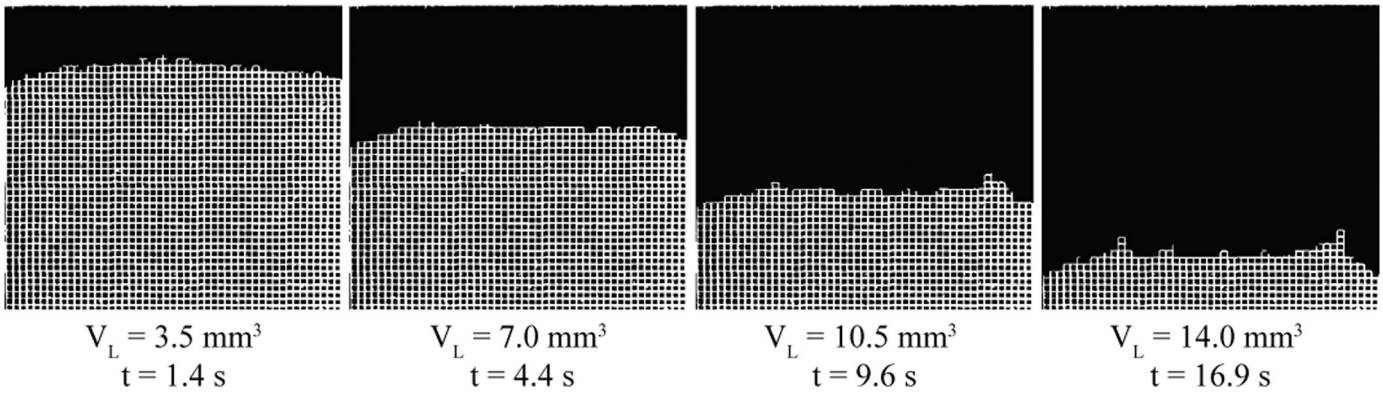


**Fig. 6.** Measured transient liquid distribution for a mixture of 40% ethanol mass fraction. Liquid-filled and empty channels are shown in black and white, respectively. The liquid front advances from the top downwards. Notice the slowing-down of the sharp interface between wet and dry regions.

It may be of interest to note that in other porous systems such as packed beds of Vycor glass beads with compact structure and well defined pores (Gruener et al., 2012), as well as highly porous silica aerogels with fractal structure (Spathis et al., 2013) the imbibition front propagates with a distinct width in which both liquid and vapor phases coexist. Detailed systematic measurements with a higher resolution digital camera and data analyses are required to characterize the width of the liquid-gas interface (i.e. interface roughness) of the propagating liquid during the process of imbibition in this specifically designed micro-model. Also, images with higher resolution can be used to characterize the imbibition process as a collection of Haines jumps (Berg et al., 2013). During imbibition process in the micro-model, capillary forces will hold up the invading liquid at the large throats. Once a throat fills, all of the pores connected to that throat fill as they are smaller in size. This jump of the position of the meniscus is called a Haines jump.

The imbibition kinetics is determined by following the liquid volume penetrated into the micro-model as a function of time for different ethanol concentrations. Since imbibition essentially occurs within very short time window, we assumed that evaporation had a negligible impact on the variation of the liquid volume in the micro-model. For all liquids, the time dependence of the advancing liquid front, quantified by the liquid volume invaded into the micro-model, follows the classical Lucas–Washburn law $V_L \propto t^{0.5}$ (Lucas, 1918; Washburn, 1921) (see Fig. 7). This power law behavior is attributed to the competition of time-invariant capillary forces driving the flow and an increasing viscous force due to the increasing length of the distances connecting the imbibition front with the liquid reservoir. This scaling behavior of the invasion front during spontaneous imbibition has also been observed in the other studies (for example, see, Gruener et al., 2012). Nevertheless we conjecture that the imbibition characteristic of the micro-model might deviate to some extent from the Lucas–Washburn law if the trapped air bubbles were taken into account in the image analysis. The role of air trapping during the wetting of microchannels shall be explored further and the results presented elsewhere at a later time.

As can be seen from Fig. 7, the imbibition rates vary among the liquid mixtures. For the 40% ethanol solution the imbibition rate is slightly higher than for the 60% ethanol solution. This observation is supported by the Lucas–Washburn law

$$l^2(t) = \frac{\sqrt{2}\sigma \cos\theta}{\mu} \bullet \sqrt{\frac{K}{\epsilon}} \bullet t, \tag{3}$$

where $\sigma$ [N/m] denotes the surface tension, $\theta$ [°] the equilibrium contact angle, and $\mu$ [Pa s] the dynamic viscosity of the liquid. $K$ [m$^2$] and $\varepsilon$ [–] denote the absolute permeability and the porosity of the micro-model, respectively. $l$ is the distance which the liquid has traveled in the network in the time $t$. The slight differences observed in the imbibition kinetics of the test liquids may be attributed to the ratio $\frac{\sigma \cos\theta}{\mu}$ which has values of about 9.8 m/s for 40%, 9.6 m/s for 60%, and 12 m/s for the 80% ethanol solution.

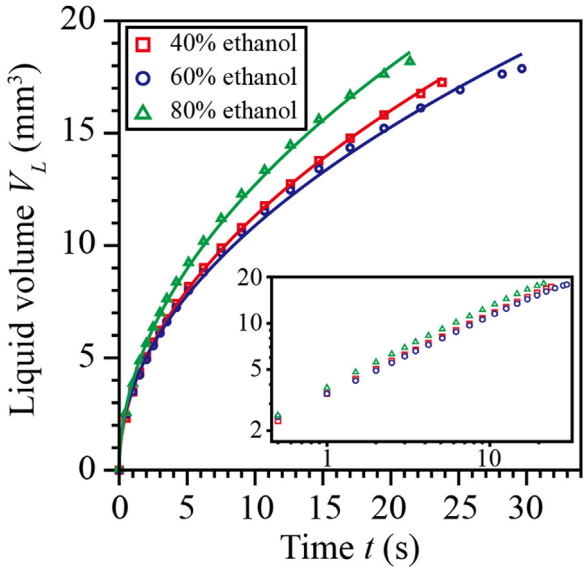


**Fig. 7.** Liquid volume $V_L$ in the micro-model for three different mixtures of water and ethanol as a function of time $t$. Measured data (symbols) are shown together with a fit $V_L \propto \sqrt{t}$ (lines). The inset shows the measured data in a log–log representation. Axes units of the inset agree with the ones of the main plot.

## 4. Pore network imbibition model

A square lattice network of throats is generated, which mimics the structural features of the micro-model used in this work. The throats are identical channels with length of 1 mm and depth of 50 μm. The throat widths are randomly distributed according to a Gaussian distribution with a mean value of 155 μm and a standard deviation of ±15 μm. The nodes at the throat junctions are without volume and form a spatial grid for the computation of the liquid pressure field. As sketched in Fig. 8, each node in the network is connected to four neighboring throats and the nodes at the top surface are connected to a liquid reservoir with a volume equal to the network void space volume. Initially the menisci are located at the entrance of surface throats in an infinitesimal distance ($\varepsilon = 10^{-9}$ m) from the surface nodes. This distance is a modeling parameter which is chosen as small as possible in order to avoid the artificial generation of significant amount of liquid. The pressure at all surface nodes is set to zero, whereas the liquid pressure in the nodes below is smaller due to capillary pressure. Because of this pressure difference, the liquid-gas interface advances through the surface throats, during which the viscous drag forces slow the liquid motion. At throat junctions, when a meniscus reaches an empty node it jumps over the node and moves over the distance $\varepsilon$ into the adjacent throat with the smallest radius, creating a new meniscus (Fig. 9a). Depending on the local pressure gradient a meniscus advances or retreats inside a throat (Fig. 9b). Two menisci coalesce when they meet in a throat (Fig. 9c). Note that maximum of two menisci is allowed to be formed in each pore throat.

During spontaneous imbibition the liquid penetrates from the top to the bottom of the network. The flow dynamics is governed by capillary pressure, viscous drag, and mass conservation. Two types of liquid menisci are modeled as the liquid penetrates into the throats. A *moving meniscus* sustains the equilibrium state of interfacial tensions between air, solid and liquid. Hence, a constant

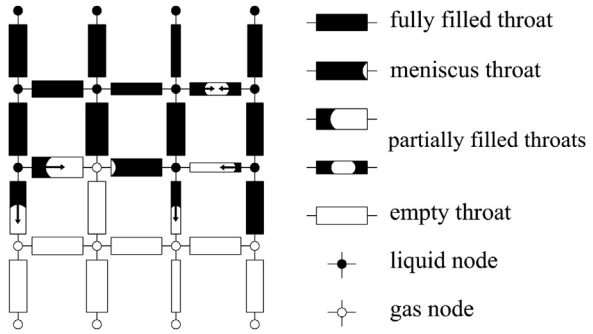


**Fig. 8.** Schematic illustration of a partially wet pore network (liquid in black, gas in white). The liquid flow direction is indicated by arrows.

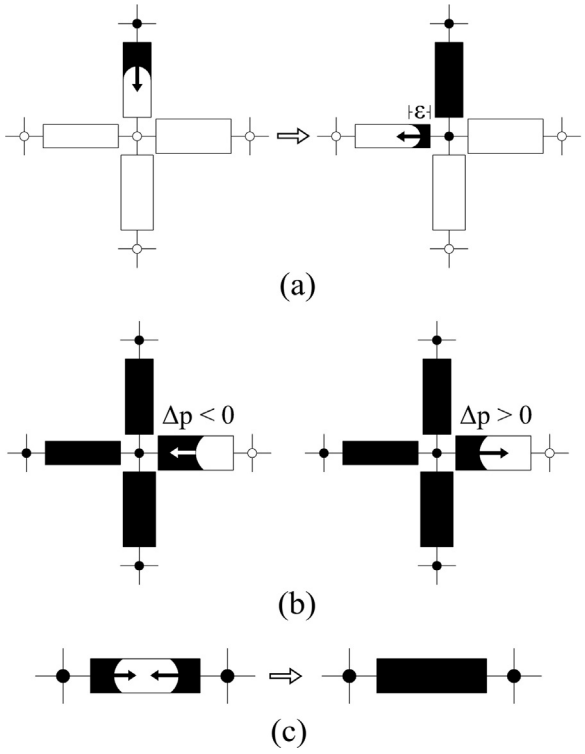


**Fig. 9.** Schematic demonstrations of pore-level transport events during spontaneous liquid imbibition. Liquid and gas are shown in black and white, respectively. Arrows inside throats indicate the liquid flow direction. (a) After reaching an empty node, the liquid immediately moves over the distance $\varepsilon$ into the adjacent throat with the smallest radius, (b) retraction of liquid towards a filled node if the driving pressure difference is negative, invasion of liquid towards an empty node if the driving pressure difference is positive, and (c) coalescence of two menisci.

(static) contact angle is applied. The capillary pressure in the throat $ij$ with a moving meniscus of radius $r_{ij}$ is computed by the Young–Laplace equation

$$P_{c,ij} = \frac{2\sigma\cos\theta}{r_{ij}}, \tag{4}$$

where $\sigma$ [N/m] denotes the surface tension, $\theta$ [°] the equilibrium contact angle. Considering the specific cross-sectional shape of the real channel (Fig. 3b), the effective radius $r_{ij}$ is calculated by

$$r_{ij} = \frac{d_{ij}(w_{ij}-d_{ij})}{w_{ij}} \tag{5}$$

where $w_{ij}$ and $d_{ij}$ denote the width and depth of the throat $ij$, respectively.

The second meniscus type is *stationary*; this type of meniscus appears only in fully filled throats. For a stationary meniscus, the pressure difference across the interface between liquid and air is small enough to prevent the liquid from receding, but too big to support the liquid invasion into the neighboring throats. Thus, no liquid flow occurs in throats with a stationary meniscus, implying that there is no liquid pressure gradient in such a throat.

This model allows for a throat to be filled or emptied depending on the local pressure gradient (Fig. 9b). In a throat, the mass flow rate of liquid $\dot{M}_{ij}$ is computed by the Hagen–Poiseuille law

$$\dot{M}_{ij} = \frac{\pi r_{ij}^4 \rho}{8\mu L_{ij} S_{ij}} \Delta P_{ij} \tag{6}$$

where $\mu$ [Pa s] denotes the dynamic viscosity of liquid, $L_{ij}$ [m] denotes the throat length, $S_{ij}$ the throat saturation, and ρ the mass density of liquid [kg/m$^3$]. The pressure difference that drives the liquid motion inside the throat $ij$ is calculated by $\Delta P_{ij}=P_i - P_{c,ij}$ or $\Delta P_{ij}=P_i - P_j$, where $P_i$ and $P_j$ denote the pressures at the nodes $i$ and $j$, respectively. The node pressures are calculated by the boundary conditions and by mass conservation. The boundary values are given by the capillary pressure at the menisci and they are equal to zero at all surface nodes, which are connected to the liquid reservoir. The mass conservation must be maintained during the entire process; at each liquid node it is determined by

$$\sum_j \dot{M}_{ij} = 0 \tag{7}$$

where the sum runs over all throats $ij$ attached to node $j$. Note that several assumptions have been made in the present pore network model: neither liquid film flow in the corners of the channels nor air trapping is considered. The gas flow at the advancing meniscus front is not modeled. The volume of pore nodes is neglected. Thermal effects are not accounted for in this model. These constrains can be relaxed with appropriate model extensions. For details on this pore network model we refer the reader to (Sun, 2014).

## 5. Pore network simulations

### 5.1. Simulation of experiments

In this section, the developed pore network model is assessed by comparing pore network simulations with micro-model measurements. The structural properties of the micro-model (see Section 2) are used to generate an equivalent pore network. The physical properties of the wetting liquid are identical to those used

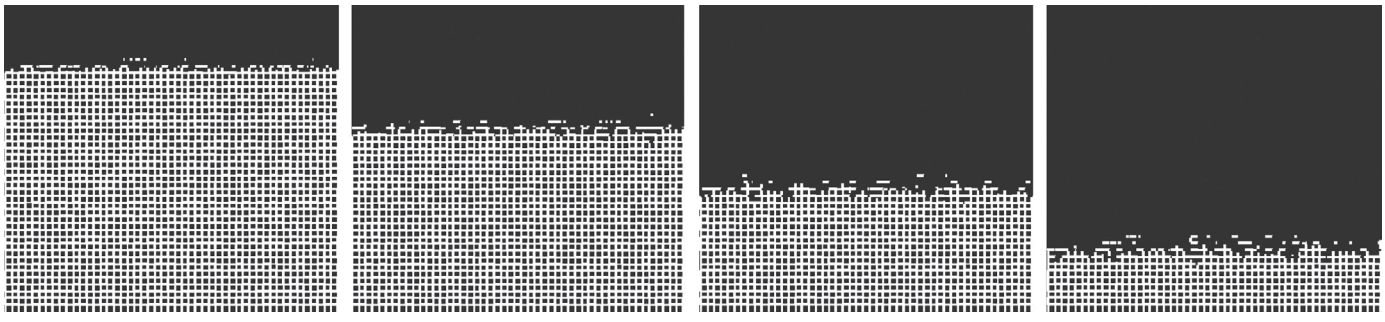


**Fig. 10.** Simulated transient liquid distribution for a mixture of 40% ethanol mass fraction. Liquid-filled and empty channels are shown in black and white, respectively. The liquid front advances downwards from the top. Notice the slowing-down of the sharp interface between wet and dry regions.

in the experiments (see Table 1). The spatial distribution of the liquid mixture with 40% ethanol mass fraction is shown in Fig. 10; similar phase distributions are obtained from the simulation with the same pore network but with different concentrations of ethanol (not shown here). The surface nodes are connected to a liquid reservoir with zero pressure. The imbibition starts from the smallest surface throats with the highest entry capillary pressures and proceeds by filling the network pore by pore with respect to their radii and their distance from the network surface. During this process, the front of the propagating liquid forms an almost continuous liquid-gas interface with finite thickness, which slightly broadens as it moves downwards. Far from the average front position the advancement of menisci is slowed down by viscous drag forces, whereas the menisci straggling behind are pulled forward by capillary forces. A similar interface characteristic has been observed in our micro-model experiments (see Fig. 6), as well as in spontaneous imbibition experiments with newspaper sheets (Miranda et al., 2010). Note that an imbibition front with a ramified structure containing arrested menisci has been observed in porous networks comprised of interconnected pores with a much higher length-to-width ratio (so-called elongated pores) (see, Gruener et al., 2012).

The time evolution of the total liquid volume inside the network for three different mixtures of water and ethanol is compared to the experimental data in Fig. 11. In general, a fairly good agreement between experiment and simulation is achieved for all test liquids, although the liquid imbibition tends to be slightly faster in the simulations. This discrepancy could be caused by certain effects that are not accounted for in the pore network model, such as the pinning behavior of liquid at the throat junctions (Shikhmurzaev and Sprittles, 2012; Wiklund and Uesaka, 2013). Due to the overlaps at the throat junctions, the total void volume of the generated pore network (22.6 $mm^3$) is about 24% more than that in the etched micro-model. As a result of this additional pore volume, the imbibition process lasts longer in the pore network simulations.

### 5.2. Further simulations and discussion

In this section, additional pore network simulations are carried out to better understand the dynamics of liquid imbibition into porous media with a bi-modal pore size distribution. For this purpose, four types of pore networks are generated in which large and small throats are spatially correlated in four different ways (Fig. 12): in networks A and B the large throats are evenly distributed in the horizontal and vertical directions, so that both the macropores and the micropores stay continuous. In network C, isolated small clusters of macropores are regularly distributed so that only the micropores form a continuous phase. In network D, a square region of large throats is generated in the center of the network.

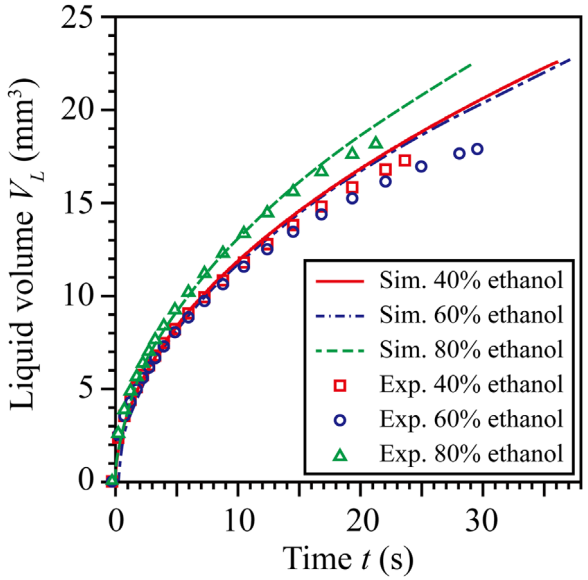


**Fig. 11.** Evolution of the liquid volume $V_L$ over time $t$ for three different mixtures of water and ethanol. Pore network simulations and micro-model measurements are shown by lines and symbols, respectively.

These four types of networks are of size $50 \times 50$ with a constant throat length of 0.4 mm. The radii of large and small throats are distributed according to normal distributions $20 \pm 2$ μm and $10 \pm 1$ μm, respectively. The volume fraction of the large throats is almost the same in all four network types, with the lowest being 23.2 % for network B and the highest being 26.9 % for network D. Note that since air entrapment is not accounted for in this model, the isolated gas throats can be fully filled with liquid during imbibition process.

Fig. 12 shows the transient liquid distributions obtained from the pore network simulations with bimodal pore size distributions. As one would expect, the small throats are preferentially invaded due to relatively high capillary pressures, leaving empty large throats behind the main imbibition front. The presence of macro channels, however, introduces a second flow domain, where the liquid moves more slowly than in the surrounding matrix of micro channels resulting in a spatially non-uniform profile. This local pattern formation in the vicinity of the imbibition front cannot be treated by macroscopic continuum models (e.g. the Lucas–Washburn law).

In Fig. 13, the simulation results are presented as liquid volume curves versus time and in Fig. 14, the transient liquid pressure fields are shown. According to Poiseuille's law, the capillary flow rate in a single throat depends on the throat radius. However, for a network of both large and small throats, the accelerating effect of large throats is much more complicated. In Fig. 13, a significant difference is found in the comparison of total imbibition times in networks A (3.16 s) and B (1.4 s). Clearly, the orientation of the large throats in the medium plays a crucial rule in accelerating the liquid imbibition. For the same fraction of large throats, the liquid flow is accelerated more in network B, where the large throats are parallel to the direction of liquid imbibition. It can be seen from Fig. 14 that a relatively high liquid pressure occurs at the throats close to the imbibition front in network B, which drives the imbibition front towards bottom.

Comparing the results for networks A and C, although half of the large throats are set to be vertical in network C, the total imbibition time (2.9 s) is only slightly reduced. The liquid pressure fields in network C indicate that the high liquid pressure is not as well sustained by the vertical large throats as it is in network B. More precisely, the high liquid pressure maintained by the vertical large throats is somewhat dissipated when the liquid flows through the small throats between the separated clusters of large throats. Hence, the continuity of the large throats also plays an important role for the imbibition rate.

For network D, the imbibition rate (see Fig. 13) is low at the beginning, but increased to a higher value when the region of large throats was filled to some extent. The total imbibition time (3.14 s) is similar as it is for network A. In fact, a continuous region of large throats serves as a barrier for the liquid flow due to the small capillary pressures. On the other hand, liquid is transported in large throats with less pressure drop. Hence, when the region of large throats is filled to a certain extent, the liquid pressure close to the imbibition front increases to support a faster movement of the imbibition front.

In Fig. 15 results of wetting simulations are shown for three

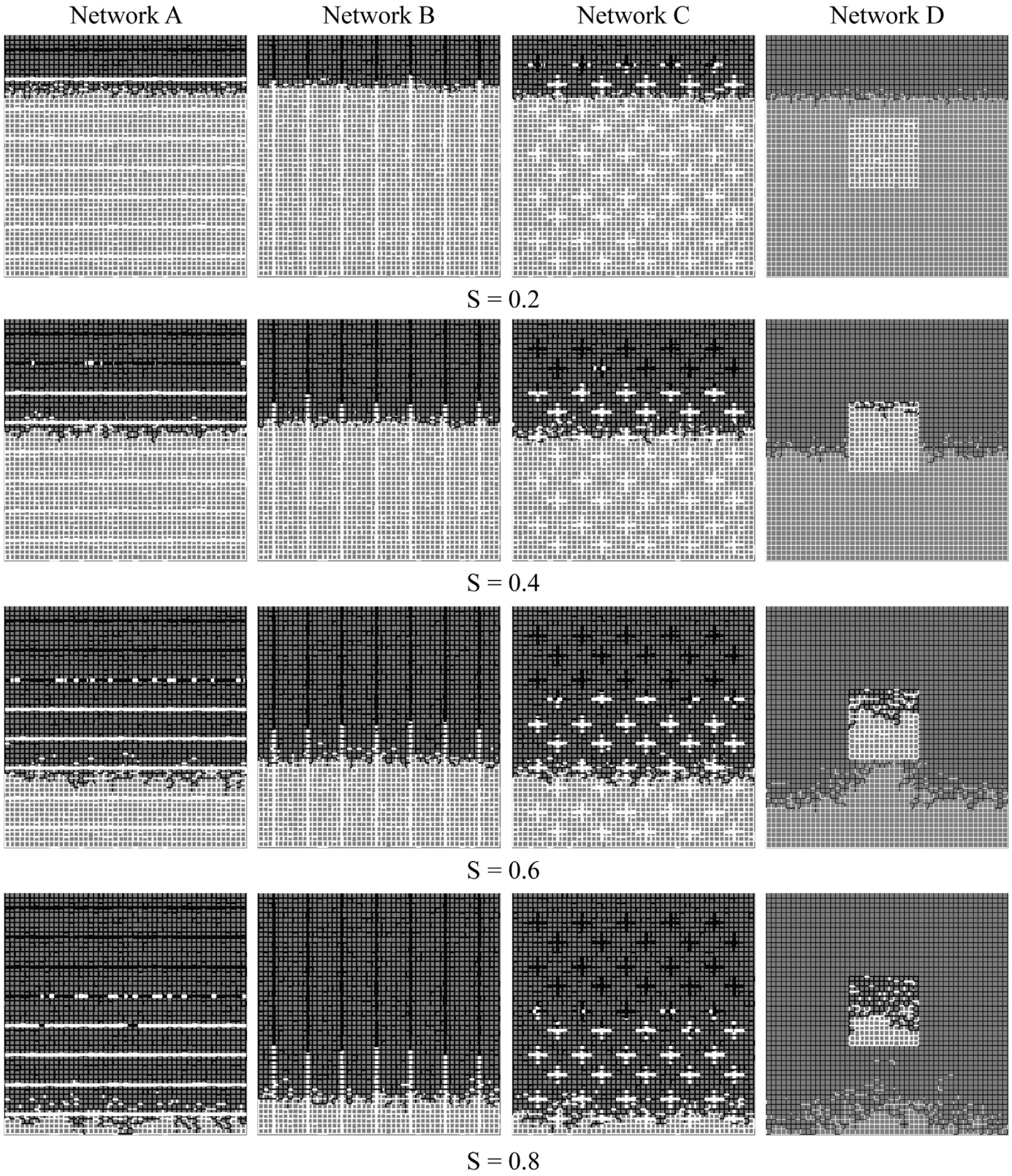


**Fig. 12.** Simulated transient liquid distribution for pore networks of types A–D at overall network saturations $S$=0.2, 0.4, 0.6, and 0.8. The liquid front advances downwards from the top (liquid shown in black, gas in white).

pore networks that have the same total size, the same total volume of throats, and individual pore diameters samples from the same mono-modal Gaussian size distribution. The only difference 5between the three networks is that they have different throat coordination numbers Z. As Fig. 15 shows, phase distributions are similar for the three networks at the same total network saturation S, whereby it should be noted that the networks are wetted from their top side, liquid-filled throats are black, and gas-filled (still empty) throats are white. The wetting front is not exactly sharp and planar, but close to this, so that description of its

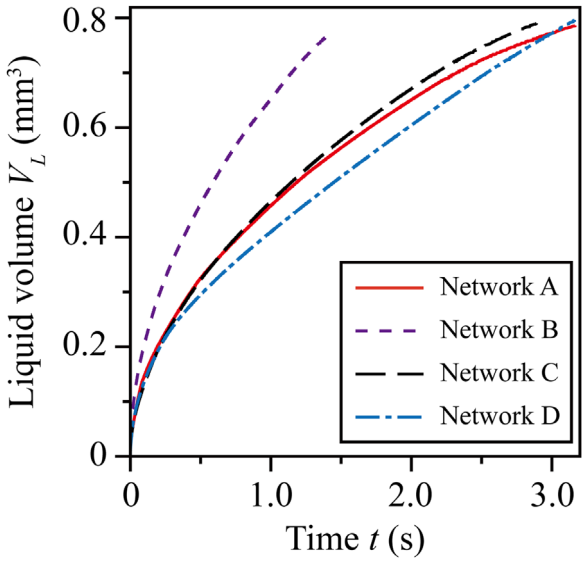


**Fig. 13.** Time evolution of the imbibed liquid volume $V_L$ for the networks of types A–D.

movement according to Washburn appears possible. However, the plot of total saturation over time in Fig. 16 reveals that a given value of S is reached earlier for a coordination number of $Z=3$ or 4, than for a coordination number of $Z=6$, meaning that the similarly looking phase distributions in Fig. 15 are reached at different times. It is clear that this cannot be described by the Washburn equation, because the underlying morphological descriptor (the coordination number $Z$) has been homogenized away in the derivation of this equation that can recognize only the average throat diameter and the average porosity of the network.

To further illustrate this issue, let us take a look at the results of Fig. 17. The respective simulations differ from the simulations used for Figs. 15 and 16 in three major ways: first, the amount of liquid made available at the top for wetting the networks was larger than network void volume in Fig. 15, but it is smaller than this in Fig. 17. Consequently, equilibrium or steady state liquid distributions that leave some throats empty are obtained at the end of the wetting process in Fig. 17. Second, the throat size distributions used to generate the networks of Fig. 17 were bimodal, consisting of small and large throats. Third, the large throats were placed in the networks of Fig. 17 by some rules of macroscopic spatial correlation: as long channels parallel to the open top of the network in network A, as long channels vertical to the open top in Network B, as regularly distributed small clusters in Network C, and as a square region in the middle of Network D. Evidently, equilibrium phase distributions and overall wetting behavior are obtained, which are utterly out of reach for the Washburn model. Such information is not only of theoretical interest and value, but it can be correlated to user properties of the product, such as solubility (Sun, 2014).

The results presented in this work clearly show that continuous models can usually describe quite well the overall kinetics of imbibition with a more or less sharp liquid front. However, continuous models cannot describe local pattern formation in the vicinity of the imbibition front, can only empirically reflect the influence of spatially uncorrelated structural features (such as the coordination number), can hardly treat wetting with liquid amounts which are small in comparison to the capacity of the porous material, and cannot treat at all spatially correlated structural features (e.g. presence of discretely or anisotropically oriented macro-pores).

Note that a pore network with a bi-modal size distribution may represent the microstructure of sedimentary rock. For such a pore structure, parameters such as the matrix sorptivities and dispersion coefficients during the spontaneous imbibition of water have been estimated so far by a 1D analytical model (Cheng et al., 2015). Although the results obtained from this simple model are

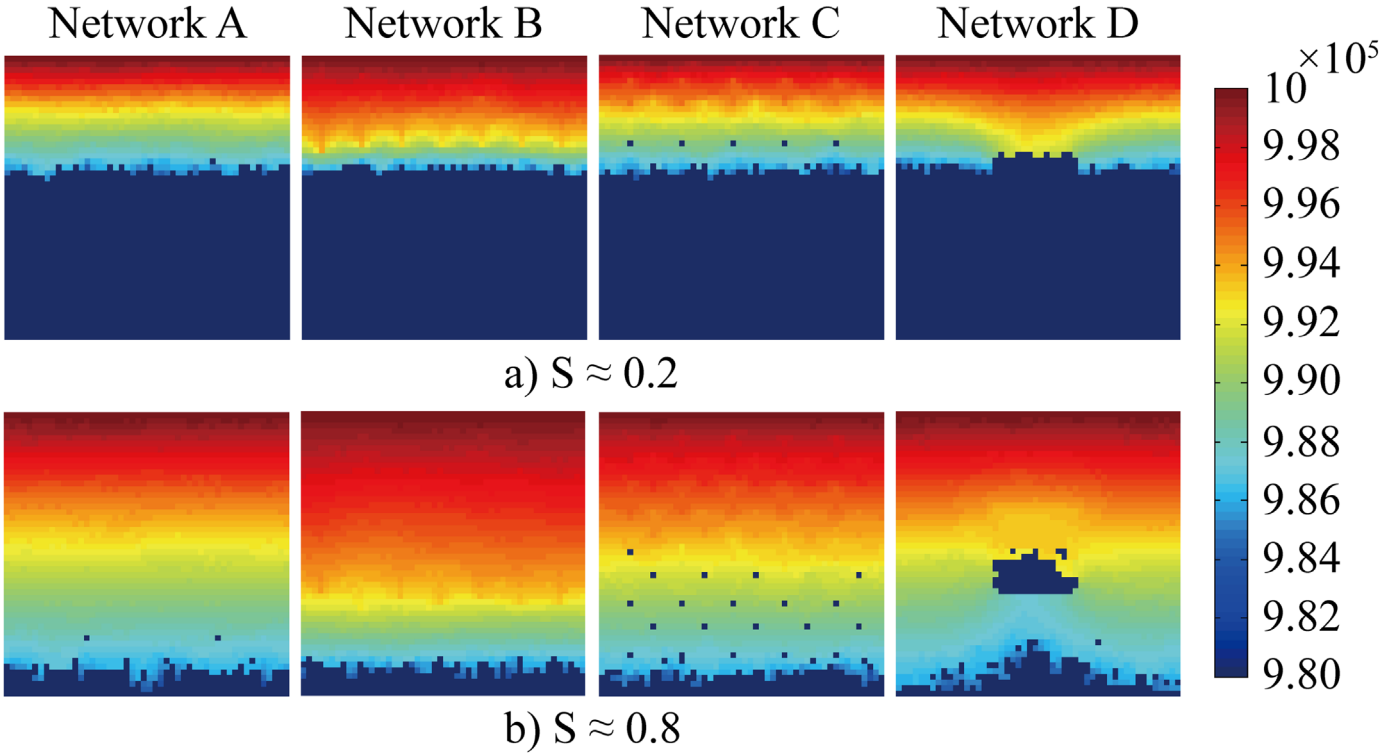


**Fig. 14.** Liquid pressure fields inside the networks A–D at overall network saturations $S \approx$ (a) 0.2, and (b) 0.8.

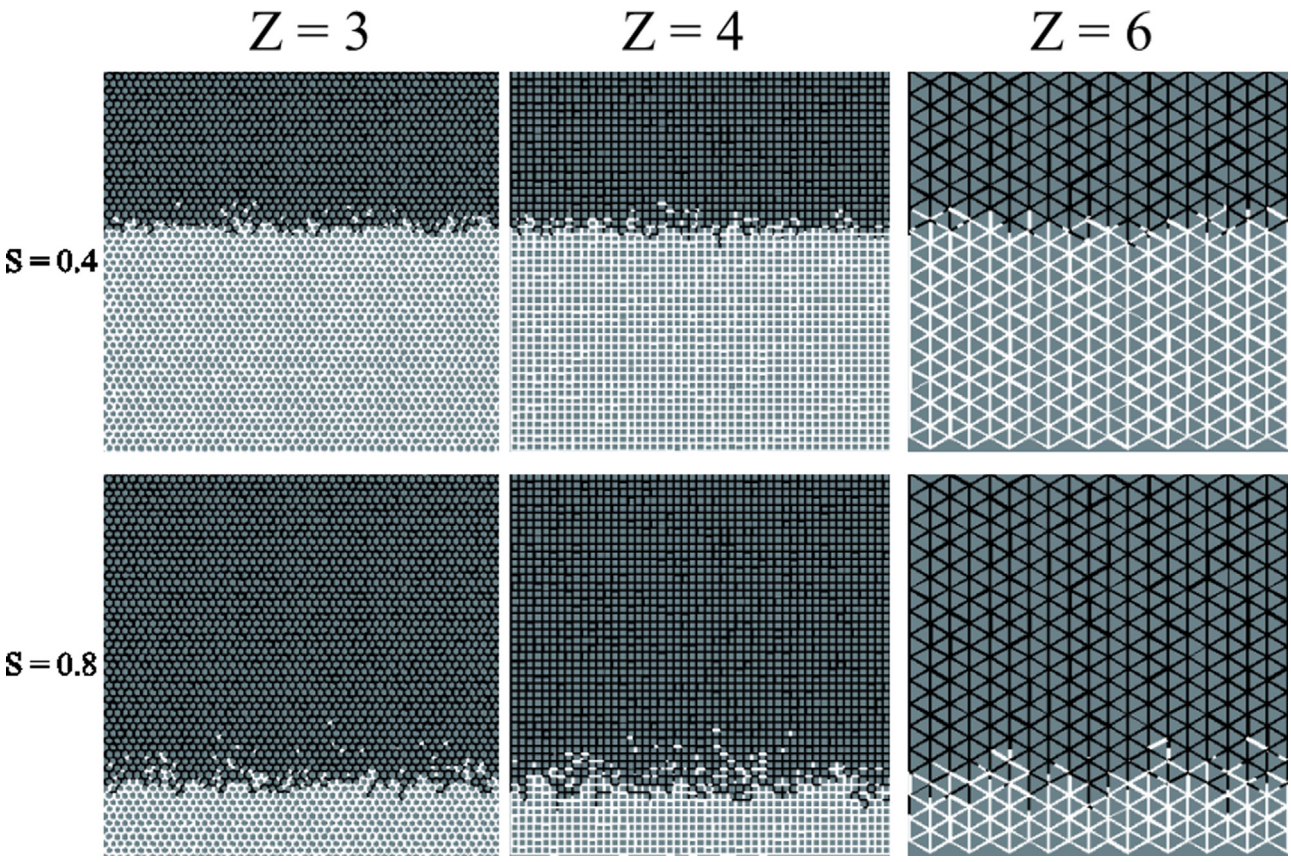


**Fig. 15.** Simulation results for the wetting of three pore networks with different throat coordination numbers *Z*.

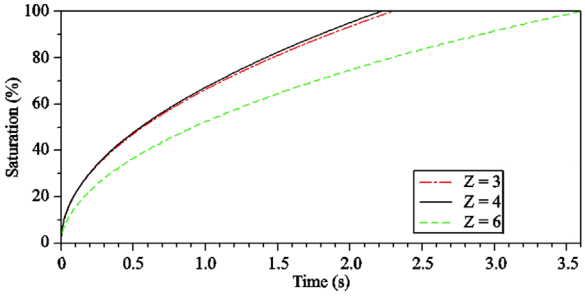


**Fig. 16.** Overall kinetics of wetting of the three pore networks with different throat coordination numbers from Fig. 15.

consistent with the experimental observations, a pore network model shall be developed to estimate these parameters for the spontaneous imbibition of porous media by numerical experiments. Also, from the numerical simulation results one may build a continuous model for estimating the effective parameters, e.g. permeability, from the micro-scale structural properties.

## 6. Summary and conclusion

Optical imbibition experiments have been successfully performed with an etched glass micro-model. For various water-ethanol mixtures, it was possible to visualize and measure the propagation features from two-dimensional images acquired by a

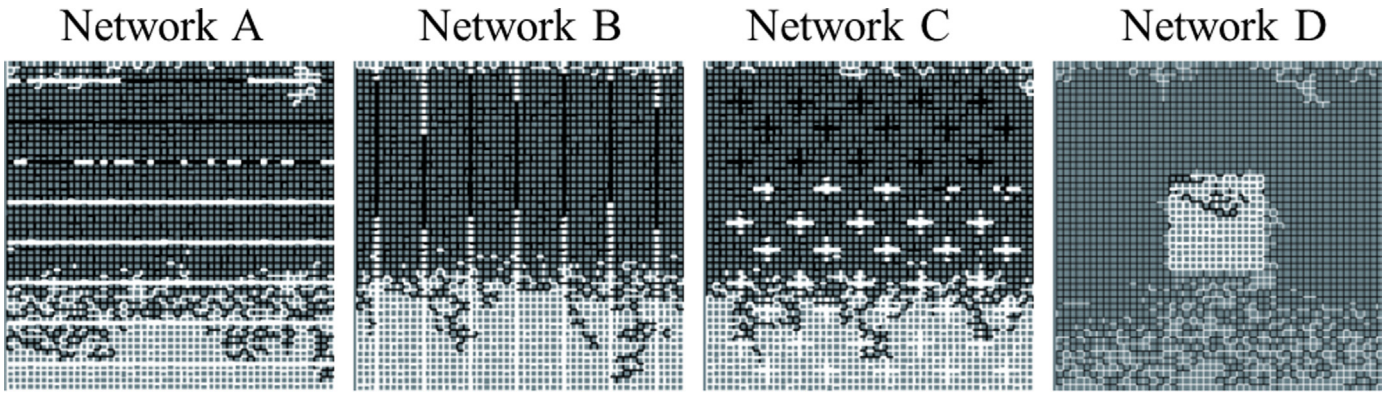


**Fig. 17.** Equilibrium liquid distributions when the volume of liquid is not sufficient for complete wetting for networks with micro-pores and spatially correlated macro-pores.

high-speed CCD camera. In this way, it could be shown that the imbibition kinetics of these water mixtures in a microfabricated network can be described by the classical Lucas–Washburn law.

A pore network was generated that could mimic the structural features of the physical micro-model. Two pore-level liquid transport rules, i.e. invasion and retraction, have been combined to determine the meniscus motion during liquid imbibition into the pore network. The experimental measurements with the micro-model are in close agreement with the pore network simulation results. Moreover, additional pore network simulations with bi-modal pore size distributions have illustrated the effect of the spatial distribution of the macro pores on the imbibition dynamics. Four types of networks with different arrangements of macro pores have been generated for this purpose. It has been observed that the overall imbibition rate strongly depends on the orientation, continuity, and cluster distribution of the macro pores. Such effects cannot be captured by the Lucas–Washburn approach.

The results in this study show that pore network modeling is a powerful tool for illustrating the imbibition dynamics in heterogeneous porous media. However, the present pore network model does not account for all relevant flow physics, such as film flow, meniscus pinning, or air entrapment. Therefore, future research shall focus on incorporating these pore-level effects into a pore network model. Furthermore, advanced micro-models consisting of more complex and realistic pore structures (e.g. a designed micro-model with bi-modal pore size distribution) shall be fabricated and used for a better assessment of the model and for the validation of simulation results.

## Acknowledgments

This work was supported by the German Research Foundation (DFG) in the framework of Graduate School 1554 “Micro-Macro-Interactions in Structured Media and Particulate Systems”. Also we are grateful to the anonymous reviewers for their valuable comments.

## References

Alava, M., Dube, M., Rost, M., 2004. Imbibition in disordered media. Adv. Phy. 53 (2), 83–175.
Al-Raoush, R.I., Willson, C.S., 2005. Extraction of physically realistic pore network properties from three-dimensional synchrotron X-ray microtomography images of unconsolidated porous media systems. J. Hydrol. 300, 44–64.
Bazylak, A., Berejnov, V., Markicevic, B., Sinton, D., Djilali, N., 2008. Numerical and microfluidic pore networks: towards designs for directed water transport in GDLs. Electrochim. Acta 53 (26), 7630–7637.
Beckingham, L.E., Peters, C.A., Um, W., Jones, K.W., Lindquist, W.B., 2013. 2D and 3D imaging resolution trade-offs in quantifying pore throats for prediction of permeability. Adv. Water Resour. 62, 1–12.
Bell, J.M., Cameron, F.K., 1906. The flow of liquids through capillary spaces. J. Phys. Chem. 10, 658–674.
Berg, S., Ott, H., Klapp, S.A., Schwing, A., Neiteler, R., Brussee, N., Makurat, A., Leu, L., Enzmann, F., Schwarz, J., Kersten, M., Irvine, S., Stampanoni, M., 2013. Real-time 3D imaging of Haines jumps in porous media flow. Proc. Natl. Acad. Sci. USA 110 (10), 3755–3759.
Blunt, M.J., 2001. Flow in porous media – pore-network models and multiphase flow. Curr. Opin. Colloid Interface Sci. 6, 197–207.
Blunt, M.J., Jackson, M.D., Piri, M., Valvatne, P.H., 2002. Detailed physics, predictive capabilities and macroscopic consequences for pore-network models of multiphase flow. Adv. Water Resour. 25, 1069–1089.
Cai, J., Perfect, E., Cheng, C.L., Hu, X., 2014. Generalized modeling of spontaneous imbibition based on Hagen–Poiseuille flow in tortuous capillaries with variably shaped apertures. Langmuir 30 (18), 5142–5151.
Cheng, J.T., Morris, J.P., Tran, J., Lumsdaine, A., Giordano, N.J., Nolte, D.D., Pyrak-Nolte, L.J., 2004. Single-phase flow in a rock fracture: micro-model experiments and network flow simulation. Int. J. Rock Mech. Min. Sci. 41 (4), 687–693.
Cheng, C.L., Perfect, E., Donnelly, B., Bilheux, H.Z., Tremsin, A.S., McKay, L.D., DiStefano, V.H., Cai, J.C., Santodonato, L.J., 2015. Rapid imbibition of water in fractures within unsaturated sedimentary rock. Adv. Water Resour. 77, 82–89.
Dullien F.A.L., 1979. Porous Media: Fluid Transport and Pore Structure, 2nd ed., Academic Press, INC., San Diego, California.
Fatt, I., 1956. The network model of porous media. AIME Pet. Trans. 207, 144–181.
Ferrari, A., Lunati, I., 2013. Direct numerical simulations of interface dynamics to link capillary pressure and total surface energy. Adv. Water Resour. 57, 19–31.
Ghassemzadeh, J., Hashemi, M., Sartor, L., Sahimi, M., 2001. Pore network simulation of imbibition into paper during coating. I Model development. AIChE J. 47, 519–535.
Ghassemzadeh, J., Sahimi, M., 2004. Pore network simulation of fluid imbibition into paper during coating—III: modelling of the two-phase flow. Chem. Eng. Sci. 59 (11), 2281–2296.
Giordano, N., Cheng, J.T., 2001. Microfluid mechanics: progress and opportunities. J. Phys.: Condens. Matter 13, R271–R295.
Gruener, S., Huber, P., 2009. Spontaneous imbibition dynamics of an *n*-alkane in nanopores: evidence of meniscus freezing and monolayer sticking. Physi. Rev. Lett. 103, 174501.
Gruener, S., Huber, P., 2011. Imbibition in mesoporous silica: rheological concepts and experiments on water and a liquid crystal. J. Phys.: Condens. Matter 23 (18), 184109.
Gruener, S., Sadjadi, Z., Hermes, H.E., Kityk, A.V., Knorr, K., Egelhaaf, S.U., Rieger, H., Huber, P., 2012. Anomalous front broadening during spontaneous imbibition in a matrix with elongated pores. Proc. Natl. Acad. Sci. USA 109 (26), 10245–10250.
Iliescu, C., Taylor, H., Avram, M., Miao, J., Franssila, S., 2012. A practical guide for the fabrication of microfluidic devices using glass and silicon. Biomicrofluidics 6, 016505.
Jazia, D.B., Vonna, L., Knopf, S., Schrodj, G., Nouali, H., Lebeau, B., Holl, Y., Haidara, H., 2013. Absorption of water/ethanol microdroplets into model porous networks. Colloids Surf. A: Physicochem. Eng. Asp. 436, 363–370.
Joekar-Niasar, V., Hassanizadeh, S.M., Pyrak-Nolte, L.J., Berentsen, C., 2009. Simulating drainage and imbibition experiments in a high-porosity micromodel using an unstructured pore network model. Water Resour. Res. 45. http://dx.doi.org/10.1029/2007WR006641.
Joekar-Niasar, V., Hassanizadeh, S.M., 2012a. Analysis of fundamentals of two-phase flow in porous media using dynamic pore-network models: a review. Crit. Rev. Environ. Sci. Technol. 42 (18), 1895–1976.
Joekar-Niasar, V., Hassanizadeh, S.M., 2012b. Effect of initial hydraulic conditions on capillary rise in a porous medium: pore-network modeling. Vadose Zone J. 11 (3). http://dx.doi.org/10.2136/vzj2011.0128.
Kang, M., Perfect, E., Cheng, C.L., Bilheux, H.Z., Gragg, M., Wright, D.M., Lamanna, J. M., Horita, J., Warren, J.M., 2013. Diffusivity and sorptivity of Berea sandstone determined using neutron radiography. Vadose Zone J. 12 (3). http://dx.doi.org/10.2136/vzj2012.0135.
Karadimitriou, N.K., Hassanizadeh, S.M., 2012. A review of micromodels and their use in two-phase flow studies. Vadose Zone J. 11 (3). http://dx.doi.org/10.2136/vzj2011.0072.
Kharaghani, A., Kirsch, C., Metzger, T., Tsotsas, E., 2013. Micro-scale fluid model for drying of highly porous particle aggregates. Comput. Chem. Eng. 52, 46–54.
Lenormand, R., Zarcone, C., Sarr, A., 1983. Mechanisms of the displacement of one fluid by another in a network of capillary ducts. J. Fluid Mech. 35, 337–353.
Leventis, A., Verganelakis, D.A., Halse, M.R., Webber, J.B., Strange, J.H., 2000. Capillary imbibition and pore characterization in cement pastes. Transp. Porous Media 39, 143–157.
Lide, D.R. (Ed.), 2010. CRC Handbook of Chemistry and Physics. CRC Press, Boca Raton, United States.
Lucas, R., 1918. Rate of capillary ascension of liquids. Kolloid Z. 23, 15–22.
Lux, J., Anguy, Y., 2012. A study of the behavior of implicit pressure explicit saturation (IMPES) schedules for two-phase flow in dynamic pore network models. Transp. Porous Media 93 (1), 203–221.
Mahmud, W.M., Nguyen, V.H., 2006. Effects of snap-off in imbibition in porous media with different spatial correlations. Transp. Porous Media 64 (3), 279–300.
Mason, G., Morrow, N.R., 2013. Developments in spontaneous imbibition and possibilities for future work. J. Pet. Sci. Eng. 110, 268–293.
MATLAB, 2013. The MathWorks, Inc., Natick, Massachusetts, United States.
Miranda, A.M., Menezes-Sobrinho, I.L., Couto, M.S., 2010. Spontaneous imbibition experiment in newspaper sheets. Phys. Rev. Lett. 104, 086101.
Montoto, M., Martineznistal, A., Rodriguezrey, A., Fernandezmerayo, N., Soriano, P., 1995. Microfractography of granitic-rocks under confocal scanning laser microscopy. Microscopy 177, 138–149.
Perrin, C.L., Tardy, P.M., Sorbie, K.S., Crawshaw, J.C., 2006. Experimental and modeling study of Newtonian and non-Newtonian fluid flow in pore network micromodels. J. Colloid Interface Sci. 295 (2), 542–550.
Piri, M., Blunt, M.J., 2004. Three-phase threshold capillary pressures in noncircular capillary tubes with different wettabilities including contact angle hysteresis. Phys. Rev. E 70, 061603.
Polzin, K.A., Choueiri, E.Y., 2003. A similarity parameter for capillary flows. J. Phys. D: Appl. Phys. 36, 3156–3167.
Porter, M.L., Schaap, M.G., Wildenschild, D., 2009. Lattice-Boltzmann simulations of the capillary pressure–saturation–interfacial area relationship for porous media. Adv. Water Resour. 32, 1632–1640.
Prodanović, M., Bryant, S.L., 2009. Physics-driven interface modeling for drainage and imbibition in fractures. SPE J. 14 (3), 532–542.
Reyssat, M., Courbin, L., Reyssat, E., Stone, H.A., 2008. Imbibition in geometries with axial variations. J. Fluid Mech. 615, 335–344.
Reyssat, M., Sangne, L.Y., Van Nierop, E.A., Stone, H.A., 2009. Imbibition in layered systems of packed beads. Europhys. Lett. 86 (5), 56002.
Sahimi, M., 1993. Flow phenomena in rocks — from continuum models to fractals, percolation, cellular-automata, and simulated annealing. Rev. Modern Phys. 65, 1393–1534.

Sahimi, M., 2011. Flow and Transport in Porous Media and Fractured Rock: From Classical Methods to Modern Approaches, 2nd ed., WILEY-VCH, Weinheim.
Serra, J., 1982. Image Analysis and Mathematical Morphology. Academic Press, New-York.
Shikhmurzaev, Y.D., Sprittles, J.E., 2012. Wetting front dynamics in an isotropic porous medium. J. Fluid Mech. 694, 399–407.
Shou, D., Ye, L., Fan, J., Fu, K., 2014. Optimal design of porous structures for the fastest liquid absorption. Langmuir 30 (1), 149–155.
Spathis, P., Delga, A., Malheiro, C., Wolf, P.E., 2013. Imbibition of liquid helium in aerogels. J. Low Temp. Phys. 171, 693–698.
Sun, Y., 2014. Liquid Imbibition in Porous Media Investigated by Pore Network Models and Pore-scale Experiments (Ph.D thesis). Otto-von-Guericke-Universität Magdeburg, Germany.
Saguy, I.S., Marabi, A., Wallach, R., 2005. Liquid imbibition during rehydration of dry porous foods. Innov. Food Sci. Emerg. Technol. 6, 37–43.
Thompson, K.E., 2002. Pore-scale modeling of fluid transport in disordered fibrous materials. AIChE J. 48, 1369–1389.
Tsakiraglou, C.D., Avraam, D.G., 2002. Fabrication of a new class of porous media models for visualization studies of multiphase flow processes. J. Mater. Sci. 37, 353–363.
Vázquez, G., Alvarez, E., Navaza, J.M., 1995. Surface tension of alcohol+water. J. Chem. Eng. Data 40, 611–614.
Van der Marck, S.C., Matsuura, T., Glas, J., 1997. Viscous and capillary pressures during drainage: network simulations and experiments. Phys. Rev. E 56, 5675–5687.
Vogel, H.J., 1997. Morphological determination of pore connectivity as a function of pore size using serial sections. Eur. J. Soil Sci. 48, 365–377.
Voronoi, G., 1908. Nouvelles applications des paramètres continus à la théorie des formes quadratiques. J. Reineund Angew. Math. 133, 97–198.
Wang, Y.J., Kharaghani, A., Metzger, T., Tsotsas, E., 2012. Pore network drying model for particle aggregates: assessment by x-ray microtomography. Dry. Technol. 30, 1800–1809.
Washburn, E.W., 1921. The dynamics of capillary flow. Phys. Rev. 17 (3), 273–283.
Wiklund, H., Uesaka, T., 2013. Microfluidics of imbibition in random porous media. Phys. Rev. E 87, 023006.
Wildenschild, D., Sheppard, A.P., 2012. X-ray imaging and analysis techniques for quantifying pore-scale structure and processes in subsurface porous medium systems. Adv. Water Resour. 51, 217–246.
Yadali Jamaloei, B., Kharrat, R., 2010. Analysis of microscopic displacement mechanisms of dilute surfactant flooding in oil-wet and water-wet porous media. Transp. Porous Media 81 (1), 1–19.
Yang, Y.W., Zografi, G., Miller, E.E., 1988. Capillary-flow and porous phenomena and wettability in porous media. 2. Dynamic flow studies. J. Colloid Interface Sci. 122, 35–46.
Young, W.B., 2004. Analysis of capillary flows in non-uniform cross-sectional capillaries. Colloids Surf. A: Physicochem. Eng. Asp. 234 (1–3), 123–128.